Efficient numerical solution of the Fokker-Planck equation using physics-conforming finite element methods

K. Wegener, D. Kuzmin, S. Turek

Efficient numerical solution of the Fokker-Planck equation using physics-conforming finite element methods

Katharina Wegener*, Dmitri Kuzmin, Stefan Turek

Institute of Applied Mathematics (LS III), TU Dortmund University, Vogelpothsweg 87, D-44227 Dortmund, Germany

---

Abstract

We consider the Fokker–Planck equation (FPE) for the orientation probability density of fiber suspensions. Using the continuous Galerkin method, we express the numerical solution in terms of Lagrange basis functions that are associated with N nodes of a computational mesh for a domain in the 3D physical space and M nodes of a mesh for the surface of a unit sphere representing the configuration space. The NM time-dependent unknowns of our finite element approximations are probabilities corresponding to discrete space locations and orientation angles. The framework of alternating-direction methods enables us to update the numerical solution in parallel by solving N evolution equations on the sphere and M three-dimensional advection equations in each (pseudo-)time step. To ensure positivity preservation as well as the normalization property of the probability density, we perform algebraic flux correction for each equation and synchronize the correction factors corresponding to different orientation angles. The velocity field for the spatial advection step is obtained using a Schur complement method to solve a generalized system of the incompressible Navier–Stokes equations (NSE). Fiber-induced subgrid-scale effects are taken into account using an effective stress tensor that depends on the second- and fourth-order moments of the orientation density function. Numerical studies are performed for individual subproblems and for the coupled FPE-NSE system.

---

*Corresponding author

Email addresses: `katharina.wegener@math.tu-dortmund.de` (Katharina Wegener), `kuzmin@math.uni-dortmund.de` (Dmitri Kuzmin), `stefan.turek@mathematik.tu-dortmund.de` (Stefan Turek)

---

1. Introduction

Coarse-grained simulations of fiber suspension flows and, in particular, of injection molding processes require accurate subgrid-scale modeling of the orientation-dependent rheology [3, 39]. Commonly used non-Newtonian flow models relate fiber-induced effective stresses to *orientation tensors*, which represent the second- and fourth-order moments of a probability density ψ. There is a one-to-one correspondence between these moments and the first coefficients of spectral (Fourier in 2D, spherical harmonics in 3D) Galerkin approximations [20, 25, 31] to the *Fokker–Planck* equation (FPE) for ψ.

Exact evolution equations for orientation tensors and for the coefficients of arbitrary-order spectral Galerkin methods can be derived from the FPE. Then a suitable *closure* approximation must be provided for the unknown high-order terms. For example, the Advani–Tucker [1] and Folgar–Tucker [11] equations for the second-order orientation tensor $\mathbf{A}(\psi)$ depend on its fourth-order counterpart $\mathbb{A}(\psi)$. Many ways to reconstruct $\mathbb{A}$ from $\mathbf{A}$ were proposed in the literature [4, 6, 9, 21, 29, 30, 34]. Lohmann [26] analyzed the resulting models, formulated criteria for physical admissibility of closures, and designed numerical methods that preserve relevant properties.

Some of the most reliable closures are based on the idea of reconstructing a probability density function ψ from $\mathbf{A}$ and using it to calculate $\mathbb{A}$. Such reconstruction-based approaches may be well suited for modeling the rheological behavior of fiber suspension flows [3, 5, 29] but the recovery of ψ from its second-order moment is an ill-posed inverse problem. Straightforward reconstruction procedures, such as the one proposed in [15], have the additional drawback that ψ may become negative. Hence, there might be no satisfactory alternative to solving the FPE, e.g., if ψ is needed to predict the mechanical properties of fiber-reinforced lightweight materials [3].

The computation of well-resolved and property-preserving numerical solutions to the FPE involves tremendous computational effort because ψ depends not only on the Cartesian coordinates of the three-dimensional physical space and on the time instant but also on two orientation angles.

2

Galerkin methods using spherical harmonics as basis functions for the configuration space [20, 25, 31] are efficient and may perform well in the diffusion-dominated regime. However, they are not to be recommended for advection-dominated transport problems because a large number of modes/moments may be needed to obtain positivity-preserving results for orientation density functions (ODFs) with sharp peaks [7]. Such ODFs correspond to strongly aligned orientation states, which frequently occur in practice.

Fractional-step methods for finite volume and finite element discretizations of the FPE and of its twin, the *Smoluchowski equation*, were developed in [2, 10, 14, 17, 18, 19, 28, 43]. Such approaches require a fine mesh resolution but, in principle, cell averages and/or pointwise values can be constrained to satisfy discrete maximum principles. In this work, we present the first high-resolution finite element scheme that ensures positivity preservation and the normalization property for numerical solutions to the FPE.

Following Knezevic [18, 19], we discretize the FPE in (pseudo-)time using an alternating-direction method. The resulting subproblems are discretized in space using the continuous Galerkin method and Lagrange finite elements. Adapting the monolithic convex limiting (MCL) procedure developed in [22], we construct an algebraic flux correction scheme that preserves all essential properties of probability density functions. The proposed algorithm is well suited for parallel computing, which is a must when it comes to putting together all building blocks of our finite element solver for the full FPE/Navier–Stokes model of fiber suspension flows. We discuss relevant implementation details and perform numerical studies for PDEs on surfaces. A test problem with a known exact solution is designed for the FPE. The results for the axisymmetric 4.5:1 contraction benchmark [24, 26, 40, 41] agree well with the numerical solutions obtained in [26] using a property-preserving finite element discretization of the Folgar–Tucker equation.

2. Mathematical modeling

Fiber suspensions are often simulated using non-Newtonian flow models in which the effective stress tensor $\boldsymbol{\tau}$ of the Navier–Stokes equations (NSE)

$$\rho \left(\frac{\partial \mathbf{v}}{\partial t} + \mathbf{v} \cdot \nabla \mathbf{v} \right) = \rho \mathbf{g} - \nabla p + \nabla \cdot \boldsymbol{\tau}, \qquad \nabla \cdot \mathbf{v} = 0 \qquad (1)$$

for the mixture velocity $\mathbf{v}$ and pressure p depends on the orientation of fibers [36]. We denote by $\mathbf{g}$ the gravitational acceleration. The mixture density ρ is assumed to be constant for simplicity. In addition to system (1), the 3D flow model that we consider includes the Fokker–Planck equation [30]

$$\frac{\partial \psi}{\partial t} + \mathbf{v} \cdot \nabla_{\mathbf{x}} \psi + \nabla_{\mathbf{p}} \cdot (\dot{\mathbf{p}} \psi) = D_r \Delta_{\mathbf{p}} \psi, \tag{2}$$

where $\psi(\mathbf{x}, \mathbf{p}, t)$ is the probability that rigid fibers located in a small neighborhood of a space location $\mathbf{x} \in \mathbb{R}^d$ have orientation $\mathbf{p} \in \mathbb{R}^d$ at time $t \geq 0$. We denote by $\nabla_{\mathbf{x}}$ or ∇ the gradient operator of the physical space $\mathbb{R}^d$ and by $\nabla_{\mathbf{p}}$ the gradient/divergence operator of the configuration space

$$\mathbb{S}^{d-1} = \{\mathbf{p} \in \mathbb{R}^d : |\mathbf{p}| = 1\}.$$

Here and below $|\cdot|$ denotes the Euclidean norm of a vector in $\mathbb{R}^d$.

The notation $\Delta_{\mathbf{p}}$ is used for the Laplace–Beltrami operator on the surface $\mathbb{S}^{d-1}$ of the unit sphere in $\mathbb{R}^d$. The *rotary diffusion* coefficient $D_r \geq 0$ measures the intensity of fiber-fiber interactions [4, 11]. The angular velocity $\dot{\mathbf{p}}$ of fiber rotation is determined by Jeffery's equation [16, 29]

$$\dot{\mathbf{p}} = \mathbf{W}\mathbf{p} + \lambda_e \left[\mathbf{D}\mathbf{p} - \mathbf{D} : (\mathbf{p} \otimes \mathbf{p})\mathbf{p}\right], \tag{3}$$

where

$$\mathbf{D} = \frac{1}{2}\left[\nabla\mathbf{v} + (\nabla\mathbf{v})^{\top}\right]$$

is the strain rate tensor,

$$\mathbf{W} = \frac{1}{2}\left[\nabla\mathbf{v} - (\nabla\mathbf{v})^{\top}\right]$$

is the spin tensor and

$$\lambda_e = \frac{r_e^2 - 1}{r_e^2 + 1}$$

is a dimensionless parameter depending on the fiber aspect ratio r_e.

A typical model for the stress tensor $\boldsymbol{\tau}$ of the NSE system is given by [36]

$$\boldsymbol{\tau} = 2\mu(\mathbf{D} + N_p \mathbb{A} : \mathbf{D} + N_s(\mathbf{D}\mathbf{A} + \mathbf{A}\mathbf{D})).$$

Here μ denotes the constant dynamic viscosity of the carrier fluid. The dimensionless parameters N_p and N_s are known as the *particle number* and *shear number*, respectively [36]. The second-order orientation tensor [1]

$$\mathbf{A}(\mathbf{x}, t) = \int_{\mathbb{S}^d} \mathbf{p} \otimes \mathbf{p} \; \psi(\mathbf{x}, \mathbf{p}, t) \, \mathrm{d}\mathbf{p} \tag{4}$$

4

and its fourth-order counterpart

$$\mathbb{A}(\mathbf{x}, t) = \int_{\mathbb{S}^d} \mathbf{p} \otimes \mathbf{p} \otimes \mathbf{p} \otimes \mathbf{p} \; \psi(\mathbf{x}, \mathbf{p}, t) \, \mathrm{d}\mathbf{p} \qquad (5)$$

satisfy evolution equations, which can be derived from (2). In this work, we evolve ψ using (2) and treat its moments as derived quantities.

For ψ to be a valid probability distribution, the admissibility conditions

$$\psi(\mathbf{x}, \mathbf{p}, t) \geq 0, \qquad \int_{\mathbb{S}^d} \psi(\mathbf{x}, \mathbf{p}, t) \, \mathrm{d}\mathbf{p} = 1 \qquad (6)$$

must hold for all $\mathbf{x} \in \mathbb{R}^d$ and $t \geq 0$. The nonnegativity of ψ implies that the symmetric tensors $\mathbf{A}$ and $\mathbb{A}$ are positive semidefinite. The normalization property implies that the trace of $\mathbf{A}$ is equal to unity. It is essential to ensure the validity of (6) for numerical solutions to (2). Otherwise, the occurrence of nonphysical orientation states may give rise to instabilities, produce misleading simulation results, or cause the code to crash.

3. Alternating-direction method

Let a finite element approximation to the solution ψ of (6) be defined by

$$\psi_h(\mathbf{x}, \mathbf{p}, t) = \sum_{i=1}^{N} \sum_{k=1}^{M} \psi_{i,k}(t) \varphi_i(\mathbf{x}) \tilde{\varphi}_k(\mathbf{p}),$$

where $\varphi_i(\mathbf{x})$ and $\tilde{\varphi}_k(\mathbf{p})$ are continuous Lagrange basis functions such that

$$\psi_{i,k}(t) = \psi_h(\mathbf{x}_i, \mathbf{p}_k, t).$$

We use linear ($\mathbb{P}_1$) finite elements on simplex meshes and multilinear ($\mathbb{Q}_1$) ones on tensor-product meshes. The degree of freedom $\psi_{i,k}(t)$ is the approximate probability of the event in which a fiber located at the ith node $\mathbf{x}_i$ of the spatial mesh has orientation $\mathbf{p}_k$ corresponding to the kth node of the surface mesh for $\mathbb{S}^{d-1}$. Using the framework of *alternating-direction* methods [12, 18, 19] to discretize the Fokker–Planck equation (6) in time, we update the entries of the coefficient matrix $\Psi = (\psi_{i,k})$ row-by-row and

column-by-column by solving simplified evolution equations for

$$\psi_{i,*}(\mathbf{p}, t) = \sum_{k=1}^{M} \psi_{i,k}(t)\tilde{\varphi}_k(\mathbf{p}), \qquad i = 1, \ldots, N,$$

$$\psi_{*,k}(\mathbf{x}, t) = \sum_{i=1}^{N} \psi_{i,k}(t)\varphi_i(\mathbf{x}), \qquad k = 1, \ldots, M.$$

To advance ψ_h in time from t^n to $t^{n+1} = t^n + \Delta t$, we need to solve the evolution equation (known as Jeffery's equation with diffusion [30])

$$\frac{\partial \psi_{i,*}}{\partial t} + \nabla_{\mathbf{p}} \cdot (\dot{\mathbf{p}} \psi_{i,*}) = D_r \Delta_{\mathbf{p}} \psi_{i,*} \tag{7}$$

for each vertex $\mathbf{x}_i$ of the spatial mesh and the advection equation

$$\frac{\partial \psi_{*,k}}{\partial t} + \mathbf{v} \cdot \nabla_{\mathbf{x}} \psi_{*,k} = 0 \tag{8}$$

for each vertex $\mathbf{p}_k$ of the spherical mesh. In the three-dimensional case, the location of $\mathbf{p}_k$ on $\mathbb{S}^3$ is determined by two orientation angles [21].

In addition to replacing (2) with a sequence of lower-dimensional subproblems that can be solved in parallel, the alternating direction (AD) approach makes it possible to discretize each subproblem using tailor-made numerical methods. We take advantage of this option in the next sections.

4. Pure advection in physical space

Let $u = \psi_{*,k}$ be the scalar-valued probability of fiber orientation along a unit vector $\mathbf{p}_k$. The second step of the AD finite element solver for (6) approximates u by a numerical solution $u_h = \sum_{j=1}^{N} u_j \varphi_j$ of

$$\frac{\partial u}{\partial t} + \mathbf{v} \cdot \nabla u = 0 \qquad \text{in } \Omega \subset \mathbb{R}^d \tag{9}$$

where $\nabla = (\partial_{x_1}, \ldots, \partial_{x_d})^\top = \nabla_{\mathbf{x}}$ is the gradient operator of the physical space $\mathbb{R}^d$ and $\mathbf{v}$ is a given divergence-free velocity field. Imposing periodic boundary conditions on $\partial\Omega$ and using the standard Galerkin method to discretize (9) in space, we obtain a linear system of the form [22]

$$\sum_{j \in \mathcal{N}_i} m_{ij} \frac{\mathrm{d}u_j}{\mathrm{d}t} + \sum_{j \in \mathcal{N}_i} a_{ij} u_j = 0, \qquad i = 1, \ldots, N, \tag{10}$$

6

where
$$m_{ij} = \int_\Omega \varphi_i \varphi_j \, \mathrm{d}\mathbf{x}, \qquad a_{ij} = \int_\Omega \varphi_i \mathbf{v} \cdot \nabla \varphi_j \, \mathrm{d}\mathbf{x}$$
are the coefficients of the consistent mass matrix and of the discrete advection operator, respectively. The integer set $\mathcal{N}_i$ contains the indices of nodes $j \in \{1, \ldots, N\}$ such that $m_{ij} \neq 0$. Introducing the notation $\dot{u}_i = \frac{\mathrm{d}u_i}{\mathrm{d}t}$ for the nodal time derivatives that appear in (9), we define
$$f_{ij} = m_{ij}(\dot{u}_i - \dot{u}_j) + d_{ij}(u_i - u_j)$$
using the artificial diffusion coefficients
$$d_{ij} = \begin{cases} \max(|a_{ij}|, |a_{ij}|) & \text{if } j \neq i, \\ -\sum_{m \in \mathcal{N}_i \setminus \{i\}} d_{im} & \text{if } j = i \end{cases}$$
and write the spatial semi-discretization (9) in the equivalent form
$$\begin{aligned} m_i \frac{\mathrm{d}u_i}{\mathrm{d}t} &= \sum_{j \in \mathcal{N}_i \setminus \{i\}} [(a_{ij} - d_{ij})(u_j - u_i) + f_{ij}] \\ &= \sum_{j \in \mathcal{N}_i \setminus \{i\}} [2d_{ij}(\bar{u}_{ij} - u_i) + f_{ij}], \end{aligned}$$
where $m_i = \sum_{j \in \mathcal{N}_i} m_{ij} = \int_\Omega \varphi_i \, \mathrm{d}\mathbf{x}$ is a positive diagonal entry of the lumped mass matrix. By definition of d_{ij}, the *bar state*
$$\bar{u}_{ij} = \frac{u_j + u_i}{2} + \frac{(a_{ij} - d_{ij})(u_j - u_i)}{2d_{ij}}$$
is a convex combination of u_i and u_j. To ensure preservation of local bounds using the *monolithic convex limiting* (MCL) algorithm proposed in [22], we replace the antidiffusive flux $f_{ij} = -f_{ji}$ with $f_{ij}^* = -f_{ji}^*$ such that
$$\min_{j \in \mathcal{N}_i} u_j =: u_i^{\min} \leq \bar{u}_{ij}^* = \bar{u}_{ij} + \frac{f_{ij}^*}{2d_{ij}} \leq u_i^{\max} := \max_{j \in \mathcal{N}_i} u_j$$
and $\bar{u}_{ji}^* \in [u_j^{\min}, u_j^{\max}]$. Under these equality and inequality constraints, the best bound-preserving approximation to f_{ij} is given by [22]
$$f_{ij}^* = \begin{cases} \min\left(f_{ij}, 2d_{ij} \min\left(u_i^{\max} - \bar{u}_{ij}, \bar{u}_{ji} - u_j^{\min}\right)\right) & \text{if } f_{ij} > 0, \\ \max\left(f_{ij}, 2d_{ij} \max(u_i^{\min} - \bar{u}_{ij}, \bar{u}_{ji} - u_j^{\max})\right) & \text{if } f_{ij} \leq 0. \end{cases}$$

If discretization is time is performed using an explicit strong stability preserving (SSP) Runge–Kutta method, and the CFL-like condition

$$\frac{2\Delta t}{m_i} \sum_{j \in \mathcal{N}_i^*} d_{ij} \leq 1$$

holds for Δt, then each forward Euler stage produces a convex combination of $u_i^{\min}$ and $u_i^{\max}$. For details, we refer the interested reader to [22].

Remark 1. The convexity-based proof of the discrete maximum principle follows the analysis of a low-order method for nonlinear hyperbolic systems in [13]. As mentioned in [22, Sec. 5.2], the MCL limiting strategy can also be used to preserve positive semi-definiteness of the second-order orientation tensor $\mathbf{A}$ in finite element discretizations of the Folgar–Tucker equation.

In the context of alternating direction methods for (2), the application of MCL to the advection equation for individual orientation modes will produce arrays of limited fluxes $f_{ij,k}^*$, $k = 1, \ldots, M$. Introducing

$$\mu_k = \int_{\mathbb{S}^{d-1}} \tilde{\varphi}_k(\mathbf{p}) \mathrm{d}\mathbf{p},$$

we impose the additional requirement that the normalization property

$$\int_{\mathbb{S}^{d-1}} \psi_{i,*}^n(\mathbf{p}) \mathrm{d}\mathbf{p} = \sum_{k=1}^{M} \mu_k \psi_{i,k}^n = 1$$

of the approximate ODF be preserved. The low-order approximations

$$\psi_{i,k}^L = \psi_{i,k}^n + \frac{\Delta t}{m_i} \sum_{j \in \mathcal{N}_i \setminus \{i\}} (d_{ij} - a_{ij})(\psi_{j,k}^n - \psi_{i,k}^n)$$

corresponding to $f_{ij}^* = 0$ meet this requirement because

$$\sum_{k=1}^{M} \mu_k \psi_{i,k}^L = \sum_{k=1}^{M} \mu_k \psi_{i,k}^n + \frac{\Delta t}{m_i} \sum_{j \in \mathcal{N}_i \setminus \{i\}} (d_{ij} - a_{ij}) \left(\sum_{k=1}^{M} \mu_k \psi_{j,k}^n - \sum_{k=1}^{M} \mu_k \psi_{i,k}^n \right)$$

$$= \sum_{k=1}^{M} \mu_k \psi_{i,k}^n = 1.$$

In view of this auxiliary result, the flux-corrected version

$$\psi_{i,k}^{\mathrm{MCL}} = \psi_{i,k}^n + \frac{\Delta t}{m_i} \sum_{j \in \mathcal{N}_i \setminus \{i\}} [(d_{ij} - a_{ij})(\psi_{j,k}^n - \psi_{i,k}^n) + f_{ij}^{**}]$$

8

satisfies the linear constraint $\sum_{k=1}^{M} \mu_k \psi_{i,k}^{\mathrm{MCL}} = \sum_{k=1}^{M} \mu_k \psi_{i,k}^{n} = 1$ if

$$\sum_{k=1}^{M} \mu_k f_{ij,k}^{**} = 0. \tag{11}$$

Adapting the scaling strategy that Lohmann et al. [27] used to enforce mass conservation in the physical space, we first calculate prelimited fluxes $f_{ij,k}^{*}$ without taking (11) into account. Then we examine the sum

$$R_{ij}^{*} = \sum_{k=1}^{M} \mu_k f_{ij,k}^{*}$$

and multiply $f_{ij,k}^{*}$ by the balancing correction factor

$$\beta_{ij,k} = \begin{cases} -\dfrac{\sum_{k=1}^{M} \min(0, \mu_k f_{ij,k}^{*})}{\sum_{k=1}^{M} \max(0, \mu_k f_{ij,k}^{*})} & \text{if } R_{ij}^{*} > 0 \text{ and } \mu_k f_{ij,k}^{*} > 0, \\ 1 & \text{if } R_{ij}^{*} = 0, \\ -\dfrac{\sum_{k=1}^{M} \max(0, \mu_k f_{ij,k}^{*})}{\sum_{k=1}^{M} \min(0, \mu_k f_{ij,k}^{*})} & \text{if } R_{ij}^{*} < 0 \text{ and } \mu_k f_{ij,k}^{*} < 0. \end{cases}$$

That is, additional limiting is performed for positive or negative components of a nonvanishing sum R_{ij}^{*} to ensure that (11) holds for $f_{ij,k}^{**} = \beta_{ij,k} f_{ij,k}^{*}$.

5. Jeffery's equation with diffusion

The MCL methodology is also applicable to finite element discretizations of PDEs on surfaces. The first step of our alternating direction method for (2) requires numerical solution of the diffusive Jeffery equation

$$\frac{\partial U}{\partial t} + \nabla_{\mathbf{p}} \cdot (\dot{\mathbf{p}} U) = D_r \Delta_{\mathbf{p}} U \qquad \text{on } \mathbb{S}^{d-1} \tag{12}$$

for the orientation states $U = \psi_{i,*}$ of mesh vertices $\mathbf{x}_k$. The representation of $\mathbf{p} \in \mathbb{S}^2$ in spherical coordinates $\phi \in [0, 2\pi)$ and $\theta \in [0, \pi]$ is given by

$$\mathbf{p} = (\sin\theta \cos\phi, \ \sin\theta \sin\phi, \ \cos\theta)^{\top}.$$

The plane tangential to $\mathbb{S}^2$ at $\mathbf{p}$ is spanned by the unit vectors

$$\mathbf{e}_\theta(\mathbf{p}) = (\cos\theta \cos\phi, \cos\theta \sin\phi, -\sin\theta)^{\top} \in \mathbb{S}^2,$$
$$\mathbf{e}_\phi(\mathbf{p}) = (-\sin\phi, \cos\phi, 0)^{\top} \in \mathbb{S}^2.$$

9

We use $\mathbf{e}_\theta$ and $\mathbf{e}_\phi$ to define the tangential gradient operator

$$\nabla_{\mathbf{p}} = \mathbf{e}_\theta \frac{\partial}{\partial\theta} + \mathbf{e}_\phi \frac{1}{\sin\theta} \frac{\partial}{\partial\phi}.$$

The surface divergence of $\mathbf{V}(\mathbf{p}) = V_\theta(\theta,\phi)\mathbf{e}_\theta(\mathbf{p}) + V_\phi(\theta,\phi)\mathbf{e}_\phi(\mathbf{p})$ is given by

$$\nabla_{\mathbf{p}} \cdot \mathbf{V} = \frac{1}{\sin\theta} \frac{\partial}{\partial\theta}(\sin\theta\, V_\theta) + \frac{\partial V_\phi}{\partial\phi}. \tag{13}$$

Let $\mathbf{V} = \nabla_{\mathbf{p}}$. Then $V_\theta = \frac{\partial}{\partial\theta}$ and $\partial V_\phi = \frac{1}{\sin\theta} \frac{\partial}{\partial\phi}$. It follows that

$$\Delta_{\mathbf{p}} = \nabla_{\mathbf{p}} \cdot \nabla_{\mathbf{p}} = \frac{\partial^2}{\partial\theta^2} + \frac{\cos\theta}{\sin\theta} \frac{\partial}{\partial\theta} + \frac{1}{\sin^2\theta} \frac{\partial^2}{\partial\phi^2}.$$

Further transformation rules of differential geometry for PDEs on surfaces can be found in [8, 42]. At the discrete level, the restriction of differential operators to elements K of a surface mesh for the manifold $\mathbb{S}^{d-1}$ is performed using a mapping $F_K : \hat{K} \to K$ from a reference element $\hat{K} \subset \mathbb{R}^{d-1}$.

Let J_K denote the Jacobian of F_K. Introducing the symmetric *Gram matrix*

$$G_K = J_K^\top J_K,$$

we use the local counterpart $\nabla_K = J_K G_K^{-1} \nabla$ of $\nabla_{\mathbf{p}}$ in the formula [42]

$$
\begin{aligned}
a_K(W,U) &= \int_{\hat{K}} \nabla_K \hat{W} \cdot (D_r \nabla_K \hat{U} - \hat{\mathbf{V}}\hat{U})\sqrt{\det G_K}\,\mathrm{d}\hat{\mathbf{x}} \\
&= D_r \int_{\hat{K}} \hat{\nabla}\hat{W} \cdot (G_K^{-1}\hat{\nabla}\hat{U})\sqrt{\det G_K}\,\mathrm{d}\hat{\mathbf{x}} \\
&\quad - \int_{\hat{K}} J_K G_K^{-1}(\hat{\nabla}\hat{W} \cdot \hat{\mathbf{V}}\hat{U})\sqrt{\det G_K}\,\mathrm{d}\hat{\mathbf{x}}
\end{aligned}
$$

for the contribution of element K to the bilinear form associated with

$$\mathcal{L}U = \nabla_{\mathbf{p}} \cdot (\mathbf{V}U - D_r\nabla_{\mathbf{p}}U).$$

The Galerkin discretization of Jeffery's equation (12) uses $\mathbf{V} = \dot{\mathbf{p}}$. The resulting semi-discrete problem can be written in the bar state form

$$\mu_k \frac{\mathrm{d}U_k}{\mathrm{d}t} = \sum_{l\in\mathcal{N}_k\backslash\{k\}} [2D_{kl}(\bar{U}_{kl} - U_k) + F_{kl} + G_{kl}], \qquad k = 1,\dots,M$$

10

and constrained using MCL to enforce preservation of local bounds. The artificial diffusion coefficients D_{kl} and the raw antidiffusive fluxes F_{kl} are defined as for the pure advection equation in $\mathbb{R}^{d-1}$. The diffusive fluxes

$$G_{kl} = D_r L_{kl}(U_l - U_k)$$

result from the discretization of $D_r\Delta_{\mathbf{p}}U$ and do not require limiting if the coefficients L_{kl} of the discrete Laplace–Beltrami operator are nonnegative for $k \neq l$. If the corresponding conditions for the geometric properties of the surface mesh are violated, the limiter should be applied to $F_{kl}+G_{kl}$. The unit sum property $\sum_{k=1}^{M} \mu_k U_k = 1$ is preserved since the Galerkin discretization of (12) is globally conservative and the limited fluxes add up to zero.

Examples of meshes that are well suited for solving PDEs on $\mathbb{S}^2$ include quadrilateral *cubed sphere* grids [32, 33] and triangular *geodesic grids* [43]. To generate a hierarchy of quadrilateral or triangular meshes for the geometric multigrid solvers implemented in our software package FEAT3, we first generate a coarse (level 0) mesh by normalizing the Cartesian coordinates of the vertices $\mathbf{X}_k$ of a cube/icosahedron containing the manifold $\mathbb{S}^2$. The cube that we use is the convex hull of the vertices $(\pm a, \pm a, \pm a)$, where $a = \frac{1}{\sqrt{3}}$. The twelve vertices of the employed icosahedron are defined by

$$(0, \pm b, \pm c), \qquad (\pm b, \pm c, 0), \qquad (\pm c, 0, \pm b),$$

where

$$b = \sqrt{\frac{2}{5 + \sqrt{5}}}, \qquad c = \frac{1 + \sqrt{5}}{\sqrt{10 + 2\sqrt{5}}}.$$

The normalized counterpart $\mathbf{x}_k = \frac{\mathbf{X}_k}{|\mathbf{X}_k|}$ of $\mathbf{X}_k \in \mathbb{R}^3$ lies on $\mathbb{S}^2$. In refinement step $m \in \mathbb{N}$, we subdivide the elements of the level $m - 1$ mesh into four subelements. The coordinates of new vertices are normalized again. Figure 1 shows the subdivision of a square/triangle and the level 4 meshes.

Remark 2. The use of (multi-)linear mappings $F_K : \hat{K} \to K$ for elements of the surface mesh may cause the discrete operators to lose some properties that are assumed in proofs of local maximum principles. Moreover, optimal convergence rates might be impossible to achieve. To avoid such troubles, we use quadratic ($\mathbb{P}_2$ or $\mathbb{Q}_2$) mappings in our finite element solver.
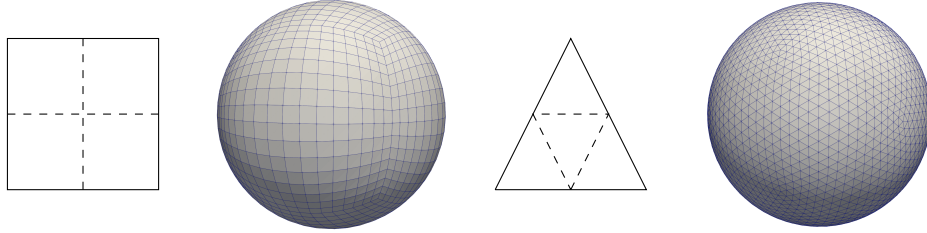
Figure 1: Refinement strategy and level 4 meshes for computations on $\mathbb{S}^2$.

6. Coupling with the flow solver

When it comes to simulating fiber suspension flows, we discretize the generalized Navier–Stokes system (1) using the inf-sup stable $\mathbb{Q}_2$-$\mathbb{P}_1^{\text{disc}}$ finite element pair (continuous $\mathbb{Q}_2$ for $\mathbf{v}$, discontinuous $\mathbb{P}_1$ for p) and solve the discrete saddle-point problem using a Schur complement method (as described in [37] and implemented in the high-performance C++ software package FEAT3). In each outer iteration or time step, a discretely divergence-free velocity field $\mathbf{v}_h$ is passed to our parallel AD solver for the Fokker–Planck equation (2). A continuous approximation $\mathbf{G}_h$ to $\nabla \mathbf{v}_h$ is recovered by minimizing the L^2 norm of $\mathbf{G}_h - \nabla \mathbf{v}_h$ subject to the incompressibility constraint $\text{tr}(\mathbf{G}_h) = 0$. The approximate probability density ψ_h is used to calculate the orientation tensors and update the effective stress tensor $\boldsymbol{\tau}$. Our implementation of the weak two-way coupling is sketched in Fig. 2.

$$
\begin{aligned}
\textbf{FPE:} \quad & \frac{\partial \psi}{\partial t} + \mathbf{v} \cdot \nabla_{\mathbf{x}} \psi + \nabla_{\mathbf{p}} \cdot (\dot{\mathbf{p}} \psi) \; = \; D_r \Delta_{\mathbf{p}} \psi, \\
& \dot{\mathbf{p}} = \mathbf{W}\mathbf{p} + \lambda_e \left[\mathbf{D}\mathbf{p} - (\mathbf{D} : (\mathbf{p} \otimes \mathbf{p})) \, \mathbf{p} \right], \\
& \mathbf{D} = \mathbf{D}(\nabla \mathbf{v}), \; \mathbf{W} = \mathbf{W}(\nabla \mathbf{v}).
\end{aligned}
$$

$$
\mathbf{v} \; \& \; \nabla \mathbf{v} \; \Uparrow \qquad\qquad \Downarrow \; \mathbf{A}(\psi) \; \& \; \mathbb{A}(\psi)
$$

$$
\begin{aligned}
\textbf{NSE:} \quad & \rho \left(\frac{\partial \mathbf{v}}{\partial t} + \mathbf{v} \cdot \nabla \mathbf{v} \right) = \rho \mathbf{g} - \nabla p + \nabla \cdot \boldsymbol{\tau}, \\
& \boldsymbol{\tau} = 2\mu (\mathbf{D} + N_p \mathbb{A} : \mathbf{D} + N_s (\mathbf{D}\mathbf{A} + \mathbf{A}\mathbf{D})), \\
& \nabla \cdot \mathbf{v} = \; 0.
\end{aligned}
$$

Figure 2: Two-way coupling for the NSE-FPE model of fiber suspension flows.

A similar fractional-step algorithm was used by Lohmann [26, Chap. 6] for a finite element discretization of the Folgar–Tucker model, in which the FPE for ψ is replaced with an evolution equation for the orientation tensor $\mathbf{A}$.

7. Numerical examples

Numerical studies of the MCL scheme for advection in the physical space were already performed in [22]. In this section, we test our finite element solvers for various equations on $\mathbb{S}^2$ and for the NSE-FPE system.

7.1. Diffusion-reaction on $\mathbb{S}^2$

We begin with an example that illustrates the importance of using at least quadratic basis functions for the mapping F_K from a planar reference element $\hat{K} \in \mathbb{R}^2$ to a curved element K of a surface mesh for $\mathbb{S}^2$. Let $U(\mathbf{p}) = p_1 p_2$ for $\mathbf{p} = (p_1, p_2, p_3)^\top \in \mathbb{S}^2$. The application of $\Delta_\mathbf{p}$ shows that U is an exact solution of the spherical diffusion-reaction equation

$$-\Delta_\mathbf{p} U + U = F \quad \text{on } \mathbb{S}^2$$

with the right-hand side $F(\mathbf{p}) = 7p_1 p_2$. We solve this elliptic problem on successively refined triangular meshes using the standard Galerkin method and $\mathbb{P}_1$ finite elements. The experimental orders of convergence (EOCs) w.r.t. the L^2 and H^1 norms are listed in Table 1. The optimal convergence rates (EOC=3.0 for the L^2 error, EOC=2.0 for the H^1 error) are achieved with $\mathbb{P}_2$ mappings. The use of $\mathbb{P}_1$ mappings decreases the EOCs by 1.0.

7.2. Heat conduction on $\mathbb{S}^2$

In the second numerical experiment, we solve the spherical heat equation

$$\frac{\partial U}{\partial t} - \Delta_\mathbf{p} U = F \text{ on } \mathbb{S}^2 \times (0, T]$$

using the manufactured exact solution $U(\mathbf{p}, t) = p_1 p_2 \exp(-t)$ to define the right-hand side $F = 5U$ and the initial data $U_0 = U(\cdot, 0)$.

Computations are performed using the Galerkin method, triangular $\mathbb{P}_1$ elements and the Crank–Nicolson time stepping. The final time is given by $T = 1.0$. The convergence history reported in Table 2 confirms that the use of $\mathbb{P}_2$ mappings is essential for achieving optimal convergence rates.

(a) linear mapping F_K

level	L^2 error	EOC	H^1 error	EOC
3	5.91e-3	-	2.14e-1	-
4	1.50e-3	1.97	2.14e-1	1.00
5	3.77e-4	1.99	5.33e-2	1.00
6	9.43e-5	1.99	2.67e-2	1.00
7	2.36e-5	1.99	1.33e-2	1.00

(b) quadratic mapping F_K

level	L^2 error	EOC	H^1 error	EOC
3	3.16e-4	-	1.13e-2	-
4	4.03e-5	2.97	2.84e-3	1.99
5	5.06e-6	2.99	7.12e-4	2.00
6	6.33e-7	3.00	1.78e-4	2.00
7	7.91e-8	3.00	4.45e-5	2.00

Table 1: Spherical reaction-diffusion equation, convergence history.

(a) linear mapping F_K

level	L^2 error	EOC	H^1 error	EOC
3	6.71e-3	-	7.66e-2	-
4	1.72e-3	1.96	3.90e-2	0.97
5	4.34e-4	1.99	1.96e-2	0.99
6	1.09e-4	2.00	9.81e-3	0.99
7	2.72e-5	2.00	4.91e-3	1.00

(b) quadratic mapping F_K

level	L^2 error	EOC	H^1 error	EOC
3	1.19e-4	-	4.15e-3	-
4	1.50e-5	2.99	1.05e-3	1.99
5	1.87e-6	3.00	2.62e-4	2.00
6	2.34e-7	3.00	6.55e-5	2.00
7	2.92e-8	3.00	1.64e-5	2.00

Table 2: Spherical heat equation, convergence history.

7.3. Pure advection on $\mathbb{S}^2$

Our next evolutionary test problem is the spherical advection equation

$$\frac{\partial U}{\partial t} + \nabla_{\mathbf{p}} \cdot (\mathbf{V}U) = 0 \quad \text{on } \mathbb{S}^2 \times (0, T].$$

Using the spherical coordinates $\theta(\mathbf{p})$ and $\phi(\mathbf{p})$, we define (cf. [23, 33])

$$V_\theta(\theta, \phi, t) = -10 \sin(2(\phi - 2\pi t)) \sin \theta \cos(\pi t),$$
$$V_\phi(\theta, \phi, t) = 20 \sin^2(\phi - 2\pi t) \cos \theta \sin \theta \cos(\pi t) + 2\pi \sin \theta.$$

By the definition (13) of the surface divergence, the velocity field

$$\mathbf{V}(\mathbf{p}) = V_\theta(\theta(\mathbf{p}), \phi(\mathbf{p}), t) \mathbf{e}_\theta(\mathbf{p}) + V_\phi(\theta(\mathbf{p}), \phi(\mathbf{p}), t) \mathbf{e}_\phi(\mathbf{p})$$

is solenoidal, i.e., $\nabla_{\mathbf{p}} \cdot \mathbf{V} = 0$. This choice of $\mathbf{V}$ results in a strong but reversible deformation of the initial data U_0. The exact solution $U(\cdot, t)$ coincides with $U(\cdot, 0) = U_0$ at the final time $T = 1$. We denote the global minimum and maximum of U_0 by $U^{\min}$ and $U^{\max}$, respectively.

Finite element approximations $U_h(\cdot, t)$ are advanced in time using an explicit second-order SSP Runge-Kutta scheme (Heun's method) and time steps Δt that satisfy appropriate CFL conditions. The global minimum and maximum of $U_h(\cdot, 1)$ are denoted by $U_h^{\min}$ and $U_h^{\max}$. The result is bound preserving if $[U_h^{\min}, U_h^{\max}] \subseteq [U^{\min}, U^{\max}]$. Let us verify if this is the case and examine the L^2 error behavior for two representative choices of U_0.

Smooth initial condition. For $\mathbf{p} = (p_1, p_2, p_3)^\top$ the initial distribution [23]

$$U_0(\mathbf{p}) = \exp\left(-5 \left((p_1 - 1)^2 + p_2^2 + p_3^2 \right) \right)$$

has the shape of a Gaussian hill. The peak is pointing in the positive p_1 direction. The range of U_0 is the interval $[U^{\min}, U^{\max}] = [0, 1]$.

The results presented in Table 3 illustrate the convergence behavior of the standard Galerkin approximation using $\mathbb{P}_2$ mappings F_K. For comparison purposes, we also report the values of $U_h^{\min}$ obtained with $\mathbb{P}_1$ mappings. The L^2 convergence rates exceed 2.0 on fine meshes. Although the bound-preserving flux limiter was deactivated in this experiment, only the result obtained on the coarsest piecewise-linear triangulation of $\mathbb{S}^2$ has a small undershoot. The snapshots displayed in Fig. 3 illustrate how the accuracy of the Galerkin approximation $U_h(\cdot, 1)$ improves as the mesh is refined.

Discontinuous initial condition. Let us now test the ability of our MCL scheme to reproduce a configuration consisting of two slotted cylinders. The

level	L^2 error	EOC	$U_h^{\max}$	$U_h^{\min}$	
				$F_K \in \mathbb{P}_1$	$F_K \in \mathbb{P}_2$
5	3.05e-01	-	0.39	-4.6e-08	2.1e-09
6	1.62e-01	0.91	0.62	2.1e-09	2.1e-09
7	5.91e-02	1.46	0.82	2.1e-09	2.1e-09
8	1.31e-02	2.18	0.93	2.1e-09	2.1e-09
9	2.24e-03	2.53	0.98	2.1e-09	2.1e-09

Table 3: Spherical advection of a Gaussian hill, convergence history.
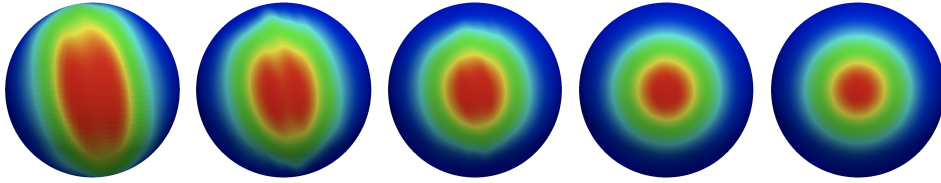
Figure 3: Spherical advection of a Gaussian hill, results for mesh levels 5–9.

initial data depicted in Fig. 4 is defined by [23, 33]

$$
U_0(\theta, \phi) = \begin{cases}
1 & \text{if } r_i \leq r \text{ and } |\phi - \phi_i| \geq \frac{r}{6} \text{ for } i = 1, 2, \\
1 & \text{if } r_1 \leq r \text{ and } |\phi - \phi_1| < \frac{r}{6} \text{ and } \theta - \theta_1 < -\frac{5}{12}r, \\
1 & \text{if } r_2 \leq r \text{ and } |\phi - \phi_2| < \frac{r}{6} \text{ and } \theta - \theta_2 > \frac{5}{12}r, \\
0 & \text{otherwise,}
\end{cases}
$$

where

$$
\begin{aligned}
r_1 &= \arccos\big(\cos\theta_1\cos\theta + \sin\theta_1\sin\theta\cos(\phi - \phi_1)\big), \\
r_2 &= \arccos\big(\cos\theta_2\cos\theta + \sin\theta_2\sin\theta\cos(\phi - \phi_2)\big).
\end{aligned}
$$

The involved constants are chosen as follows:

$$
r = \frac{1}{2}, \quad \theta_1 = \theta_2 = 0, \quad \phi_1 = \frac{5\pi}{6}, \quad \phi_2 = \frac{7\pi}{6}.
$$

The exact solution $U(\cdot, 1) = 1$ is again bounded by $U^{\min} = 0$ and $U^{\max} = 1$.

In this experiment, we constrain the baseline Galerkin discretization using MCL. The effect of mesh refinement on the L^2 and L^∞ errors is illustrated by the data presented in Table 4. The small negative values of $U_h^{\min}$ are due to the fact that our surface triangulations do not reproduce $\mathbb{S}^2$ exactly. As already mentioned, mapping errors may result in a loss of some matrix
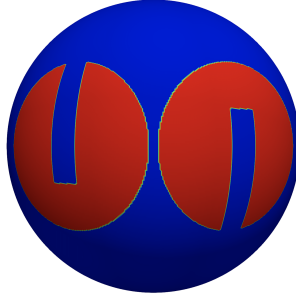
16

Figure 4: Spherical advection of slotted cylinders, initial data.

properties that are assumed in proofs of discrete maximum principles for flux-corrected Galerkin methods. The magnitude of the undershoots in our numerical results for the advection of slotted cylinders decreases as the order of the mapping F_K is increased and/or the mesh is refined. The L^2 error decreases so slowly because the exact solution is discontinuous. Figure 5 shows the MCL solutions $U_h(\cdot, 1)$ calculated on mesh levels 5–9.

level	L^2 error	EOC	$U_h^{\max}$	$U_h^{\min}$	
				$F_K \in \mathbb{P}_1$	$F_K \in \mathbb{P}_2$
5	0.74	-	0.72	-1.3e-06	-3.6e-07
6	0.58	0.35	0.97	-1.0e-07	-3.1e-08
7	0.45	0.38	1.00	-1.4e-08	-4.6e-09
8	0.33	0.45	1.00	-1.8e-09	-5.7e-10
9	0.24	0.42	1.00	-2.2e-10	-7.2e-11

Table 4: Spherical advection of slotted cylinders, convergence history.
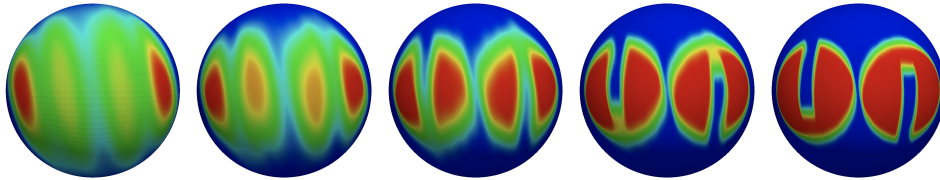
Figure 5: Spherical advection of slotted cylinders, results for mesh levels 5–9.

7.4. Fokker–Planck equation

In the first three examples, we considered test problems with known solutions. To design such a test problem for the Fokker–Planck equation (2), we

17

assume that ψ depends only on the first two components of $\mathbf{x} = (x, y, z)^\top$ and that the probability $u(\mathbf{x}, t) = \psi(\mathbf{x}, \mathbf{p}, t)$ of any particular orientation $\mathbf{p} \in \mathbb{S}^2$ satisfies the two-dimensional linear advection problem

$$\frac{\partial u}{\partial t} + \mathbf{v} \cdot \nabla u = 0 \qquad \text{in } \Omega = \{(x, y) \in \mathbb{R}^2 : x^2 + y^2 < 1\}$$

with the solenoidal velocity field $\mathbf{v}(x, y) = (-y, x)^\top$ that corresponds to solid body rotation about the center of the spatial domain Ω.

In the Lagrangian reference frame that rotates with the velocity $\mathbf{v}$, the Fokker–Planck equation (2) reduces to Jeffery's equation (12). We define the velocity $\dot{\mathbf{p}}$ of spherical advection using the constant tensors

$$\mathbf{D} = \frac{1}{2}\left[\nabla \mathbf{u} + (\nabla \mathbf{u})^\top\right], \qquad \mathbf{W} = \frac{1}{2}\left[\nabla \mathbf{u} - (\nabla \mathbf{u})^\top\right]$$

that represent the symmetric and skew-symmetric part of

$$\nabla \mathbf{u} = \text{diag}(0.02, -0.01, -0.01).$$

In the case $D_r = 0$, an exact solution of Jeffery's equation is given by [29]

$$U(\mathbf{p}, t) = U_0\left(\frac{\mathbf{C}(t)\mathbf{p}}{|\mathbf{C}(t)\mathbf{p}|}\right)\frac{1}{|\mathbf{C}(t)\mathbf{p}|^3},$$

where $\mathbf{C}(t) = \exp\left(-t(\mathbf{W} + \lambda_e \mathbf{D})\right)$ and

$$U_0(\mathbf{p}) = \frac{1}{4\pi|\mathbf{C}(t_0)\mathbf{p}|^3}.$$

For $t_0 = 0$ this definition of U_0 corresponds to the assumption of an isotropic initial distribution. Let us define the initial condition

$$\psi_0(\mathbf{x}, \mathbf{p}) = \frac{1}{4\pi|\mathbf{C}(t_0(\mathbf{x}))\mathbf{p}|^3}$$

using $t_0(\mathbf{x}) = x$. At the final time $T = 2\pi$, the exact solution

$$\psi(\mathbf{x}, \mathbf{p}, T) = \frac{1}{4\pi|\mathbf{C}(x + T)\mathbf{p}|^3}$$

of the Fokker–Planck equation (2) coincides with the result $\hat{\psi}(\mathbf{x}, \mathbf{p}, T)$ of solving Jeffery's equation in the rotating Lagrangian reference frame (or, equivalently, with the exact solution to (2) using $\mathbf{v} = \mathbf{0}$).

The snapshots shown in the top row of Fig. 6(a) are the results $\psi_{*,2}(\cdot, t)$ of an Eulerian simulation for $\mathbf{v}(x, y) = (-y, x)^\top$. In Fig. 6(b), we present the corresponding snapshots for a Lagrangian simulation, in which the physical advection step of the alternating direction method was skipped. The good agreement between the last diagrams of each row indicates that the discretization of the advective term $\mathbf{v} \cdot \nabla \psi$ does not introduce significant additional errors. The results of detailed grid convergence studies performed in [42] reveal that the L^2 error of the Eulerian and Lagrangian approximations to $\psi(\mathbf{x}, \mathbf{p}, 2\pi) = \hat{\psi}(\mathbf{x}, \mathbf{p}, 2\pi)$ exhibits second-order convergence even if we start with a spatially discontinuous orientation distribution.

(a) Eulerian version (Fokker–Planck equation for ψ)
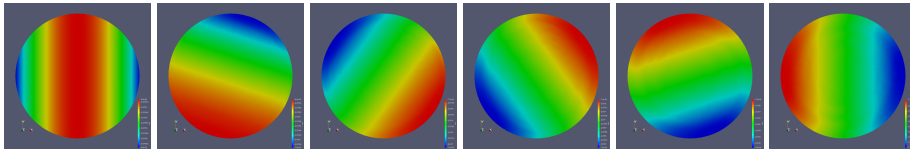
(b) Lagrangian version (Jeffery's equation for $\hat{\psi}$)
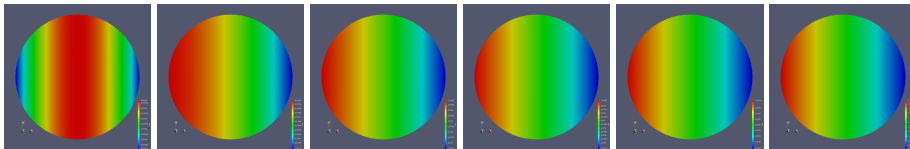
Figure 6: Solid body rotation, $\psi_{*,2}(\cdot, t)$ at $t \in \left\{0, \frac{2}{5}\pi, \frac{4}{5}\pi, \frac{6}{5}\pi, \frac{8}{5}\pi, 2\pi\right\}$, mesh level 7.

7.5. Axisymmetric contraction

It remains to test the two-way coupling of our finite element solvers for the Fokker–Planck equation (2) and for the Navier–Stokes system (1). A well-known benchmark for fiber suspension flows is the axisymmetric 4.5:1 contraction problem. For a detailed description of the initial-boundary value problem and of the computational setup, we refer the reader to [26, 40, 41]. Experimentally measured velocity fields and numerical simulation results for flows of fibers through axisymmetric contractions can be found in [24].

In our numerical experiments, we define the rotary diffusion rate

$$D_r = C_I \sqrt{\mathbf{D} : \mathbf{D}}$$

19

using $C_I = 0.002$. Further parameter settings are as follows:

$$\lambda_e = \frac{99}{101}, \quad \rho = 1, \quad \mu = 0.1, \quad N_s = 0, \quad N_p = 6.$$

Since $N_s = 0$, the formula for the effective stress tensor $\boldsymbol{\tau}$ simplifies to

$$\boldsymbol{\tau} = 2\mu(\mathbf{D} + N_p \mathbb{A} : \mathbf{D})$$

and only the fourth-order moment $\mathbb{A}(\psi_h)$ of the approximate probability density ψ_h needs to be passed to the Navier–Stokes solver. The list of derived quantities that we calculate and output in the postprocessing stage includes the second-order orientation tensor $\mathbf{A}(\psi_h)$. This enables us to compare our simulation results with numerical solutions published in [26, 40, 41].

The hexahedral meshes on which we solve the NSE system and evolve the orientation modes $\psi_{*,k}$ in the physical space are generated from the coarse mesh shown in Fig. 7. In Figs 8 and 9, we present the stationary velocity field and snapshots of the maximum eigenvalue of $\mathbf{A}(\psi_h)$. These results are in good agreement with those obtained by Lohmann [26] using a physics-compatible finite element discretization of the Folgar–Tucker equation.
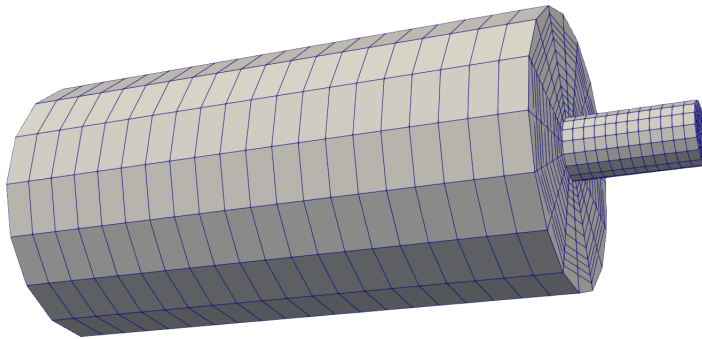

Figure 7: Axisymmetric contraction, coarse mesh for the spatial domain.

8. Conclusions

The methodology presented in this paper provides a fail-safe numerical tool for computational exploration of evolving orientation states in suspensions of fibers or rod-like molecules. The proposed extension of monolithic convex
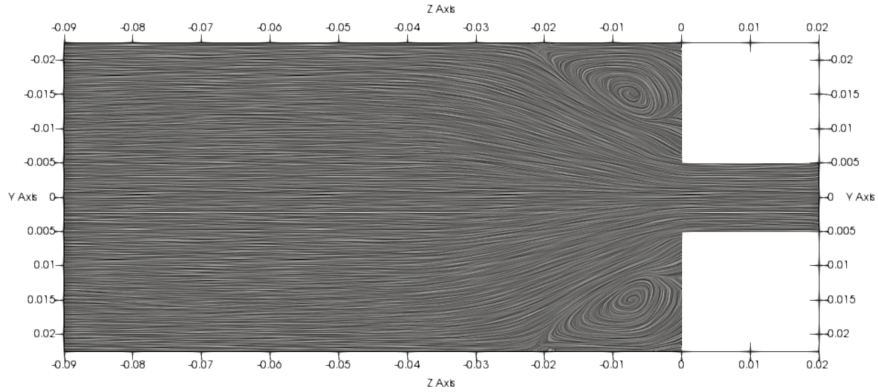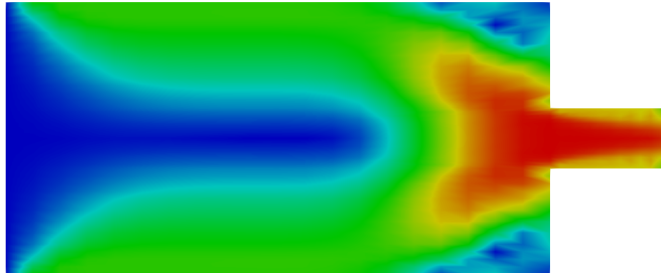
Figure 8: Axisymmetric contraction, stationary velocity field.

limiting techniques to a finite element discretization of the Fokker–Planck equation guarantees positivity preservation and the normalization property. We are not aware of any other work that is focused on the aspects of limiting for the FPE. The modular design of our fractional-step algorithm makes it possible to improve the accuracy and efficiency of individual subproblem solvers step-by-step. The developed software can be used to validate closure models or generate snapshots/dictionaries for reduced-order modeling. Further effort is needed to enhance the computational performance because millions of discrete unknowns need to be updated in each time step. Our experience with other applications indicates that the use of GPU acceleration [38] and machine learning tools [35] may result in significant speedups.
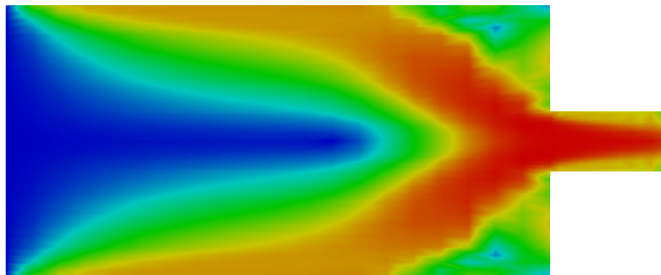
Acknowledgments

(a) $t = 1.25$

(b) $t = 6.25$

(c) $t = 25.0$
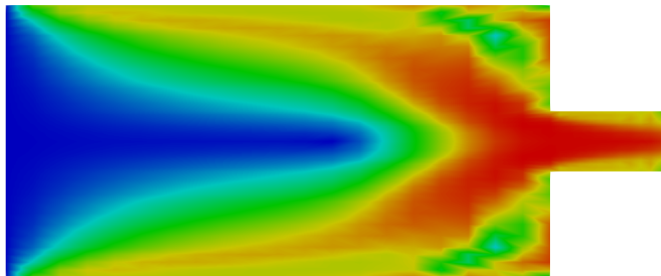

Figure 9: Axisymmetric contraction, maximum eigenvalue of the orientation tensor **A**.

References

[1] S.G. Advani and C.L. Tucker, The use of tensors to describe and predict fiber orientation in short fiber composites. *J. Rheol.* **31** (1987) 751–784.

[2] N.A. Al Ayoubi, H. Digonnet, L.R. Da Silva, C. Binetruy, T. Renault, and S. Comas-Cardona, Simulation of the fiber orientation through a

finite element approach to solve the Fokker–Planck equation. Available at SSRN: `http://dx.doi.org/10.2139/ssrn.4216630`.

[3] K. Breuer, M. Stommel, and W. Korte, Analysis and evaluation of fiber orientation reconstruction methods. *J. Compos. Sci.* **3** (2019) 67.

[4] J.S. Cintra and C.L. Tucker III, Orthotropic closure approximations for flow-induced fiber orientation. *J. Rheol.* **39** (1995) 1095–1121.

[5] C.V. Chaubal and L.G. Leal, A closure approximation for liquid-crystalline polymer models based on parametric density estimation. *J. Rheol.* **42** (1998) 177–201.

[6] D.H. Chung and T.H. Kwon, Improved model of orthotropic closure approximation for flow induced fiber orientation. *Polymer Composites* **22** (2001) 636-649.

[7] S. Dahm and C. Helzel, Hyperbolic systems of moment equations describing sedimentation in suspensions of rod-like particles. *Multiscale Modeling & Simulation* **20** (2022) 1002—1039.

[8] G. Dziuk and C. M. Elliott, Finite element methods for surface PDEs. *Acta Numerica* **22** (2013) 289–396.

[9] F. Dupret and V. Verleye, Modelling the flow of fiber suspensions in narrow gaps. *Advances in the Flow and Rheology of Non-Newtonian Fluids* **8** (1999) 1347–1398.

[10] J. Férec, D. Mezi, S. G. Advani, and Gilles Ausias, Axisymmetric flow simulations of fiber suspensions as described by 3D probability distribution function. *Journal of Non-Newtonian Fluid Mechanics* **284** (2020) 104367.

[11] F.P. Folgar and C.L. Tucker III, Orientation behavior of fibers in concentrated suspensions. *Journal of Reinforced Plastics and Composites* **3** (1984) 98–119.

[12] S. Ganesan, Operator-splitting finite element algorithms for computations of high-dimensional parabolic problems. *Applied Math. & Computation* **219** (2013) 6182–6196.

[13] J.-L. Guermond and B. Popov, Invariant domains and first-order continuous finite element approximation for hyperbolic systems. *SIAM J. Numer. Anal.* **54** (2016) 2466–2489.

[14] C. Helzel and F. Otto, Multiscale simulations for suspensions of rod-like molecules. *J. Comput. Phys.* **216** (2006) 52–75.

[15] D.A. Jack and D.E. Smith, Assessing the use of tensor closure methods with orientation distribution reconstruction functions. *Journal of Composite Materials* **38** (2004) 1851–1871.

[16] G.B. Jeffery, The motion of ellipsoidal particles immersed in a viscous fluid. *Proc. Roy. Soc. Lon* **A102** (1922) 161–179.

[17] T. Johnson, P. Röyttä, A. Mark, and F. Edelvik, Simulation of the spherical orientation probability distribution of paper fibers in an entire suspension using immersed boundary methods. *Journal of Non-Newtonian Fluid Mechanics* **229** (2016) 1–7.

[18] D. Knezevic, Finite element methods for deterministic simulation of polymeric fluids. Report NA-06/19, Oxford University Computing Laboratory, Numerical Analysis Group, 2006.

[19] D. Knezevic, *Analysis and Implementation of Numerical Methods for Simulating Dilute Polymeric Fluids.* PhD thesis, University of Oxford, 2008.

[20] D. Knezevic and E. Süli, A heterogeneous alternating-direction method for a micro-macro dilute polymeric fluid model. *ESIAM: M2AN* **43** (2009) 1117–1156.

[21] D. Kuzmin, Planar and orthotropic closures for orientation tensors in fiber suspension flow models. *SIAM Journal on Applied Mathematics* **78** (2018) 3040–3059.

[22] D. Kuzmin, Monolithic convex limiting for continuous finite element discretizations of hyperbolic conservation laws. *Comput. Methods Appl. Mech. Engrg.* **361** (2020) 112804.

[23] P.H. Lauritzen, W.C. Skamarock, M.J. Prather, and M.A. Taylor, A standard test case suite for two-dimensional linear transport on the sphere. *Geoscientific Model Development* **5** (2012) 887–901.

[24] G.G. Lipscomb II, M.M. Denn, D.U. Hur, D.V. Boger, The flow of fiber suspensions in complex geometries. *Journal of Non-Newtonian Fluid Mechanics* **26** (1998) 297–325.

[25] C. Lohmann, Efficient algorithms for constraining orientation tensors in Galerkin methods for the Fokker-Planck equation. *Computers & Mathematics with Applications* **71** (2016) 1059–1073.

[26] C. Lohmann, *Physics-Compatible Finite Element Methods for Scalar and Tensorial Advection Problems.* Springer Spektrum, 2019.

[27] C. Lohmann, D. Kuzmin, J.N. Shadid and S. Mabuza, Flux-corrected transport algorithms for continuous Galerkin methods based on high order Bernstein finite elements. *J. Comput. Phys.* **344** (2017) 151–186.

[28] A. Masud and L. A. Bergman, Application of multi-scale finite element methods to the solution of the Fokker-Planck equation. *Computer Methods Appl. Mech. Engrg. 194* (2005) 1513–1526.

[29] S. Montgomery-Smith, W. He, D. A. Jack, and D. E. Smith, Exact tensor closures for the three-dimensional Jeffery's equation. *J. Fluid Mech.* **680** (2011) 321–335.

[30] S. Montgomery-Smith, D. Jack, and D. E. Smith, The fast exact closure for Jeffery's equation with diffusion. *Journal of Non-Newtonian Fluid Mechanics*, **166** (2011) 343–353.

[31] S. Montgomery-Smith, D. A. Jack, and D. E. Smith, A systematic approach to obtaining numerical solutions of Jeffery's type equations using Spherical Harmonics. In: *Composites Part A: Applied Science and Manufacturing* **41** (2010) 827–835.

[32] R.D. Nair, S. J. Thomas, and R.D. Loft, A discontinuous Galerkin transport scheme on the cubed sphere. *Monthly Weather Review* **133** (2005) 814–828.

[33] K. Peterson, P. Bochev, and D. Ridzal, Optimization-based conservative transport on the cubed-sphere grid. In: I. Lirkov, S. Margenov, J. Wasniewski (Eds), *International Conference on Large-Scale Scientific Computing*, Springer, 2013, pp. 205–212.

[34] E. Pruliére, A. Ammar, and F. Chinesta, Empirical natural closure relation for short fiber suspension models. *International Journal of Forming Processes* **10** (2007) 1292–7775.

[35] H. Ruelmann, M. Geveler, D. Ribbrock, P. Zajac, and S. Turek, Basic machine learning approaches for the acceleration of PDE simulations

and realization in the FEAT3 Software. In: F. Vermolen and C. Vuik (eds), *Numerical Mathematics and Advanced Applications* (Proceedings of ENUMATH 2019), Springer, 2020.

[36] C. L. Tucker III, Flow regimes for fiber suspensions in narrow gaps. *J. Non-Newtonian Fluid Mechanics* **39** (1991) 239–268.

[37] S. Turek, *Efficient Solvers for Incompressible Flow Problems: An Algorithmic and Computational Approach*, LNCSE <u>6</u>, Springer, 1999.

[38] S. Turek, D. Göddeke, S. Buijssen, and H. Wobker, Hardware-oriented multigrid finite element solvers on (GPU)-accelerated clusters. In: J. Kurzak, D. A. Bader, J. Dongarra (eds), *Scientific Computing with Multicore and Accelerators*. CRC Press, 2010, chapter 6, 113–130.

[39] V. Verleye and F. Dupret, Prediction of fiber orientation in complex injection molded parts. In: D. A. Siginer (Ed.), *Developments in Non-Newtonian Flows*, AMD-Vol. **175**, ASME 1993, pp. 139–163.

[40] B.E. VerWeyst, *Numerical Predictions of Flow-Induced Fiber Orientation in Three-Dimensional Geometries*. PhD thesis, University of Illinois, 1998.

[41] B.E. VerWeyst and C.L. Tucker III, Fiber suspensions in complex geometries: Flow/orientation coupling. *Canadian J. Chem. Eng.* **80** (2002) 1093–1106.

[42] K. Wegener, *Efficient Numerical Solution of the Fokker–Planck Equation Using Physics-Conforming Finite Element Methods*. PhD thesis, TU Dortmund University, to be submitted in 2023.

[43] E. Zharovsky, A. Moosaie, A. Le Duc, M. Manhart, and B. Simeon, On the numerical solution of a convection-diffusion equation for particle orientation dynamics on geodesic grids. *Appl. Numer. Math.* **62** (2012) 1554–1566.